ACS OMEGA

http://pubs.acs.org/journal/acsodf

Article

Facile Fabrication of Durable Biochar/H_2-TiO_2 for Highly Efficient Solar-Driven Degradation of Enrofloxacin: Properties, Degradation Pathways, and Mechanism

Ji Shi, Wenyu Huang,* Hongxiang Zhu, Jianhua Xiong, Huiting Bei, and Shuangfei Wang*

Cite This: *ACS Omega* 2022, 7, 12158−12170

Read Online

ACCESS | Metrics & More | Article Recommendations | Supporting Information

ABSTRACT: Widespread application of TiO_2 for degradation of antibiotics is restricted by mainly the low photodegradation efficiency under solar irradiation. To expand the application of TiO_2, the key factors that should be improved are visible-light response, yield of electrons and holes, and durability. Herein, we report a visible-light responsive and durable sugarcane-bagasse-derived biochar supported hydrogenated TiO_2 (HSCB/H_2-TiO_2) photocatalyst with higher electron production fabricated by a facile one-pot hydrogenation. Mild hydrogenation temperature preserved the lotus-stem-like structure of sugarcane bagasse and gave the photocatalyst great separability. The superior durability of HSCB/H_2-TiO_2 was demonstrated by 12 rounds of repeated degradation of methylene blue (MB). In addition, the electron paramagnetic resonance (EPR) results demonstrated that the biochar skeleton contains abundant persistent free radicals (PFRs), which can provide excess electrons to form more $^{\bullet}O_2^-$. Meanwhile, radical quenching experiment and EPR radical trapping results also revealed that $^{\bullet}O_2^-$ was the most dominant species for enrofloxacin (ENR) degradation. Thus, the as-fabricated photocatalyst shows excellent solar-driven degradation of ENR, and 95.6% of ENR was degraded in 180 min under simulated solar irradiation. Possible ENR degradation pathways and mechanism are also proposed based on the identified intermediates.

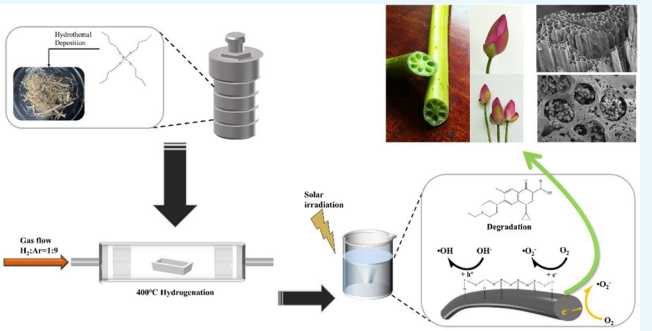

1. INTRODUCTION

Water, one of the most fundamental renewable natural resources, is essential for human health.[1] Over 70% of human weight consists of water. Despite abundant water resources, only 2.5% of water is drinkable. Antibiotics in water worsen the shortage of drinking water. Fluoroquinolones (FQs), one of the most consumed antibiotics in the world, are of special concern because they have been shown to be genotoxic in samples from hospital wastewaters. Enrofloxacin (ENR), a commonly used veterinary FQ, is of greater interest in environmental systems because of its environmental accumulation, poor biodegradability, high adsorption affinity, and the long-term chronic effects at low concentrations in water.[2,3] In recent years, adsorption,[4] electrocatalysis,[5] photocatalysis,[6] and photoelectrocatalysis[5] have been developed to successfully alleviate the pollution from ENR. However, most of them cannot achieve cost efficient[2,7] and ecofriendly[2] operation simultaneously. Solar-driven photocatalysis using semiconductor materials seems to be a promising method to remove ENR in water owing to its high efficiency, relatively favorable cost−performance ratio, and it is free of unstable oxidants. Moreover, most solar-driven catalysts designed for water purification are solids, allowing them to be easily separated and recycled.[8,9]

TiO_2 is a promising semiconductor photocatalyst.[10,11] Great accessibility and relatively low environmental toxicity allow its wide application in antibiotics degradation.[12] However, the poor solar response of TiO_2 significantly limits its photoefficiency.[13] Only 4% of total solar energy, mostly UV light, can be utilized by TiO_2,[14] thus severely restricting its widespread application. Bandgap narrowing is one of the most promising methods to enhance the response to visible irradiation.[15] We reported that hydrogenation and fluorine doping could increase the solar-driven degradation performance of TiO_2 particles to varying degrees.[9] Han's team dispersed Pt/black TiO_2 onto a light-diffuse-reflection surface to demonstrate highly efficient photocatalytic steam reforming of methane. The yield of H_2 under visible-light irradiation increased by 3-fold compared to previous reports.[16]

Another major drawback of TiO_2 particles is their low yield of electrons. Although electrons can be excited from the

Received: January 26, 2022
Accepted: March 14, 2022
Published: March 28, 2022

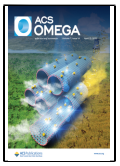

valence band of TiO_2, they quickly recombine with holes and are not able to form reactive oxygen species (ROS). The high electron−hole recombination rate severely restricts the yield of light-induced electrons. Yang et al. reported a carbothermal reduction induced Ti^{3+} self-doped TiO_2/graphene quantum dot (GQD) nanohybrid. Citric acid was used as the organic source in their study. The nanohybrid showed better photoinduced charge generation and enhanced charge transport on the surface layer.[17] Besides use as an electron−hole separator, carbon-based materials were also used as a crystal growth controller. Yang et al. found that TiO_2 nanoparticles deposited on a cellulose surface were spindle-like and had very low agglomeration.[18]

Modifying TiO_2 with biochar, a carbon-rich, low-cost product derived from the pyrolysis of biomass with limited oxygen, is an optimal solution to the drawbacks discussed above. Different sources of biochar modified TiO_2 are now a rising stars in water and air purification,[19] soil remediation,[20] and the semiconductor industry[21] because of their excellent conductivity and high radiation adsorption.[22,23] Moreover, persistent free radicals (PFRs) are generated during the formation of biochar, which can increase the formation of $^{\bullet}O_2^-$ in heterogeneous degradation.[24] Sugarcane bagasse (SCB), one of the most critical and abundant organic byproducts of the sugar industry,[25] is an ideal organic source of carbon. However, biochar modified TiO_2 suffers from a major drawback, which is poor durability. It is difficult to control the mass loss during repeated tests because of either small particle size or the fragility of the biochar skeleton. Shen et al.[8] decorated biochar with magnetic materials to increase the separation ability of composites. Although the magnetic absorbent can be easily separated from the solution using a magnet, the addition of magnetic materials increases the cost of manufacture.

In this report, we synthesized a visible-light responsive and durable sugarcane-bagasse-derived biochar supported hydrogenated TiO_2 (HSCB/H_2-TiO_2) photocatalyst via one-pot hydrogenation. The morphology and chemical composition of the photocatalyst were characterized thoroughly. Its solar-driven degradation performance toward ENR and durability were systematically studied. The yield of $^{\bullet}OH$ and $^{\bullet}O_2^-$ were evaluated and compared, and the contribution of different ROS to ENR degradation was determined. Finally, the degradation intermediates of ENR were identified, and a possible mechanism of ENR degradation by HSCB/H_2-TiO_2 was proposed based on the results.

2. EXPERIMENTAL SECTION

2.1. Chemical Reagents. Predried SCB (average length 2 cm) was obtained from Nanhua Sugar Mill, Guangxi, China. Hydrogen peroxide (H_2O_2, AR, 30%) was purchased from Chuandong Chemical, Chongqing, China. Glacial acetic acid (CH_3COOH, AR, 99.5%) was purchased from Damao Chemical, Tianjin, China. Titanium butoxide ($Ti(BuO)_4$, AR, 99.0%), tertiary butyl alcohol (TBA, $C_4H_{10}O$, AR), tryptophan (Trp, AR), trichloromethane ($CHCl_3$, AR), $AgNO_3$ (AR), dimethylpyridine nitrogen oxide (DMPO, AR), 2,2,6,6-tetramethylpiperidine (TEMP, AR), 2,2,6,6-tetramethylpiperidine nitrogen oxide (TEMPO, AR), and ENR ($C_{19}H_{22}FN_3O_3$, AR) were purchased from Aladdin, Shanghai, China. Ethanol (CH_3CH_2OH, AR, 99.5%) was purchased from Fuyu Fine Chemical, Tianjin, China. All chemical reagents were used as received without further purification. Deionized water was used in this study.

2.2. Preparation of SCB/TiO_2 Composites. First, SCB was soaked in a premixed H_2O_2/CH_3COOH solution (H_2O_2/CH_3COOH = 1:1, v/v), and the solution was magnetically stirred for 30 min at 25 °C. Then, the solution was transferred to a 60 °C water bath for 12 h. After thorough washing with deionized water, the pretreated SCB was oven-dried at 80 °C for 24 h. Next, SCB/TiO_2 composites were prepared via a simple hydrothermal process. Typically, 2 g of pretreated SCB was soaked in 150 mL of ionized water followed by the addition of 60 mL of ethanol. Then, 12.5 mL of $Ti(BuO)_4$ was slowly injected (2 drops/s) to the mixture under vigorous magnetic stirring. After 30 min reaction, the obtained creamy solution and SCB were transferred to a Teflon-lined autoclave and subjected to a 24 h hydrothermal process to synthesize SCB/TiO_2. The hydrothermal temperature was set at 160 °C. The SCB/TiO_2 was washed three times with deionized water and then dried in an oven at 80 °C for 24 h.

2.3. Preparation of HSCB/H_2-TiO_2 Photocatalyst. The as-obtained SCB/TiO_2 composites were subjected to a mild one-pot hydrogenation process (H_2/Ar volume ratio was 1:9, and hydrogenation temperature was 400 °C) for 3 h. Hydrogenation was performed in a silica tube furnace at ambient pressure. The silica tube diameter was 90 mm and length was 800 mm. To eliminate the effect of oxygen, the furnace was ventilated with a H_2−Ar mixed gas for 15 min prior to the heating. The gas flow rate was set to 600 μL/s, and the temperature ramp rate was set to 5 °C/min. Finally, the as-prepared synchronous hydrogenated biochar/H_2-TiO_2 was naturally cooled to room temperature. Plain hydrogenated biochar was prepared following the same hydrogenation process. Pure TiO_2 and H_2-TiO_2 particles were prepared following our previous method.[9]

2.4. Characterization. The specific surface area was determined by N_2 adsorption−desorption isotherm using a Micromeritics ASAP 2460 instrument and calculated by BET method. The surface morphology and lotus-stem-like multichannel structure were observed using a scanning electron microscope (SEM, Zeiss Sigma 300). The elemental composition of a selected area was characterized using an energy-dispersive X-ray spectrometer (EDS, Zeiss SmartEDX). The morphology of HSCB/H_2-TiO_2 composites was observed by high-resolution transmission electron microscopy (HRTEM, FEI Tecnai G2 F20 S-TWIN) with an acceleration voltage of 200 kV. The X-ray diffraction (XRD) patterns of samples were obtained using a D/MAX 2500 V X-ray diffractometer (Rigaku, Japan) in the 2θ range of 10−90° and at a scanning rate of 5°/min. The surface functional groups of biochar and HSCB/H_2-TiO_2 were characterized by Fourier transform infrared spectroscopy (FT-IR, SHIMADZU IR-Trace-100). The core level Ti 2p, O 1s, and C 1s spectra were determined by X-ray photoelectron spectroscopy (XPS, Thermo Fisher Scientific ESCALAB 250XI+). The amount of PFRs in the HSCB were determined from electron paramagnetic resonance (EPR) spectra recorded using a Bruker E580 spectrometer (Germany).

2.5. Measurement of Photodegradation-Related Properties. EPR radical trapping tests were conducted on a Bruker E580 spectrometer (Germany) with DMPO, TEMP, and TEMPO as spin-trapping agents. Radical quenching experiments were carried out to determine the dominant ROS in the ENR degradation. HSCB/H_2-TiO_2 was used as photocatalyst, and $CHCl_3$, $AgNO_3$, Trp and TBA were used as scavengers for $^{\bullet}O_2^-$ and $^{\bullet}OH^-$, respectively. To visualize the

https://doi.org/10.1021/acsomega.2c00523
ACS Omega 2022, 7, 12158−12170

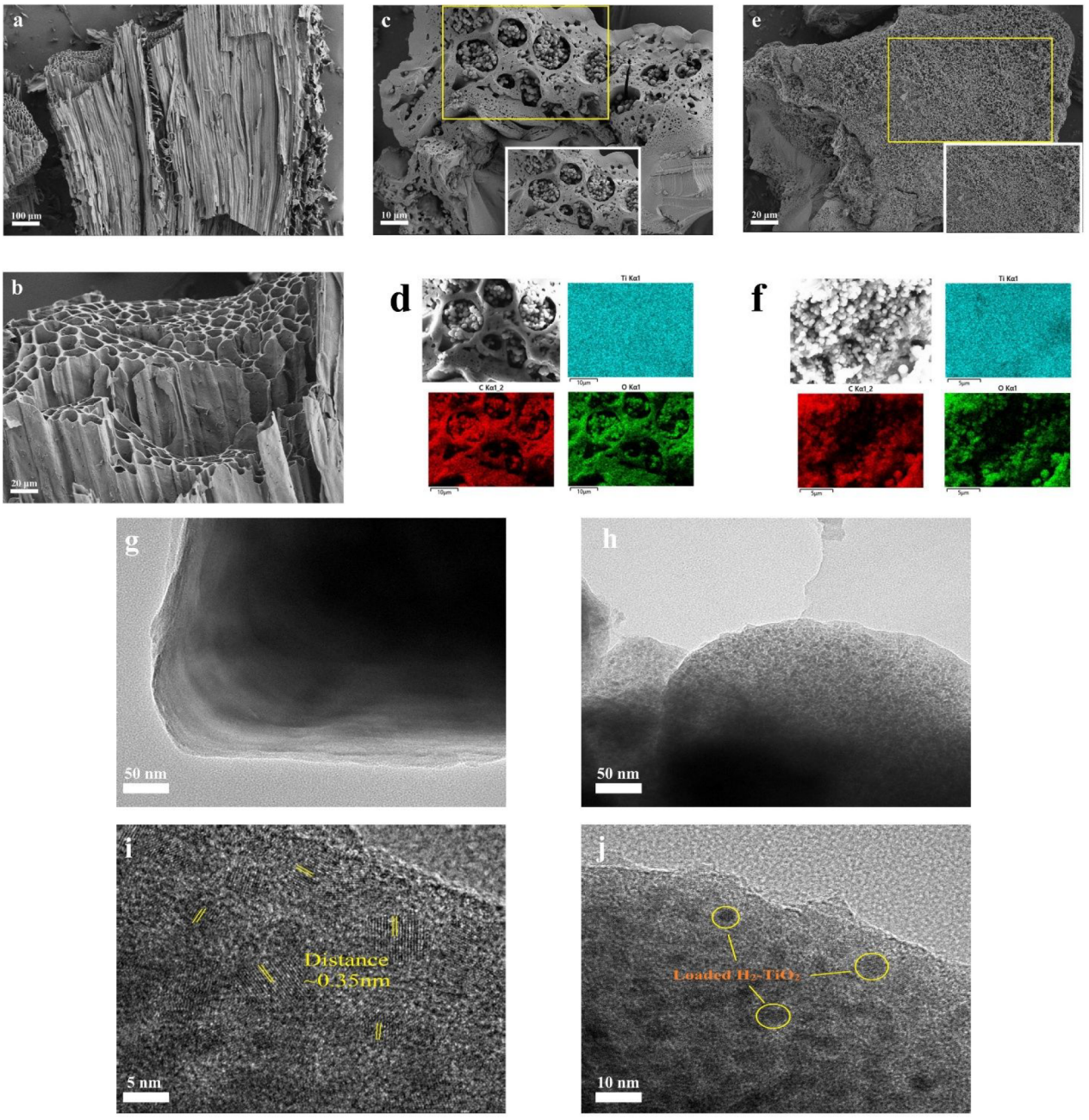

Figure 1. (a, b) SEM images of HSCB. (c) SEM image of the front end of HSCB/H_2-TiO_2; insets, enlarged images of the selected (yellow square) area. (d) EDS elemental mapping of corresponding insets. (e) SEM image of the side wall of HSCB/H_2-TiO_2. (f) EDS elemental mapping of corresponding insets. (g) TEM image of HSCB. (h–j) TEM images of HSCB/H_2-TiO_2 with different magnifications.

electron–hole recombination rate, steady and transient photoluminescence (PL) emission spectra were obtained with a Hitachi F7100 with 330 nm light excitation. Contact angle tests were carried out using a JY-82B Kruss DSA goniometer under solar irradiation to determine the hydrophilicity/hydrophobicity of HSCB/H_2-TiO_2 composites and H_2-TiO_2 particles. The sessile drop method was used, and an adjustable plane parallel backlight was used as the source of solar irradiation. Transient photocurrent and Mott–Schottky plot of HSCB/H_2-TiO_2 composites and H_2-TiO_2 particles were recorded using an electrochemical workstation (Shanghai Chenhua, CHI 760E). Specifically, HSCB/H_2-TiO_2 and H_2-TiO_2 were ground and dispersed in ethanol. After 30 min sonication, the dispersed liquid was coated on the ITO substrate and calcined at 400 °C to remove impurities. The curves of transient photocurrent vs time (I–t curves) were recorded using a standard three-electrode system (Pt was used as the counter electrode, Ag/AgCl was used as the reference electrode, and the photocatalyst-coated ITO was used as the working electrode) with periodic on/off illumination. The on/off cycle was set for 10 s. The electrolyte was 1 mol/L Na_2SO_4 aqueous solution, and a broadband 250 W xenon lamp (consisting of 9% UV, 43% visible light, and 48% infrared light) was used as the light source.

2.6. Solar-Driven Catalytic Degradation of ENR and Durability Tests. For the degradation of ENR, the typical process was that 20 mg of HSCB/H_2-TiO_2 (containing 0.25 mg of H_2-TiO_2) was first dispersed and soaked in 200 mL of

https://doi.org/10.1021/acsomega.2c00523
ACS Omega 2022, 7, 12158–12170

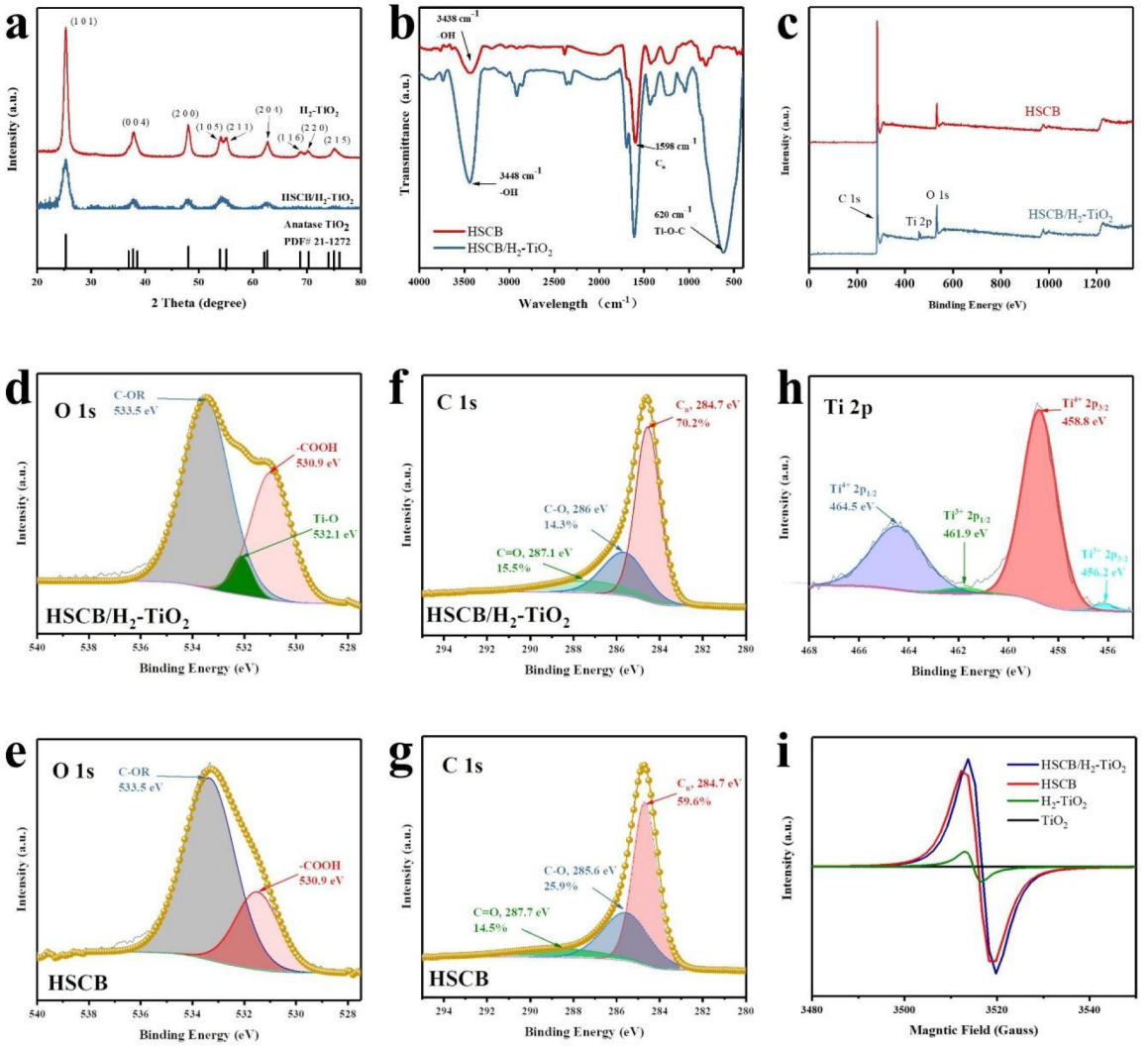

Figure 2. (a) XRD patterns of H_2-TiO_2 and HSCB/H_2-TiO_2. Pattern of anatase TiO_2 is shown as reference. (b, c) FT-IR spectra and XPS full scan, respectively, of HSCB and HSCB/H_2-TiO_2. (d, e) High-resolution XPS O 1s spectra of HSCB/H_2-TiO_2 and HSCB, respectively. The deconvoluted results are shown as shaded regions. (f, g) High-resolution C 1s XPS spectra and the deconvoluted results for HSCB/H_2-TiO_2 and HSCB, respectively. (h) High-resolution Ti 2p XPS spectrum of HSCB/H_2-TiO_2. (i) Solid state EPR results of different samples.

3.6 mg/L ENR solution with magnetic stirring in the dark for 2 h to reach the adsorption−desorption equilibrium. The sample was then transferred to a transparent cylindrical glass reactor. The wall of the reactor was filled with circulating cooling water to maintain the reactor at room temperature. A broadband 250 W xenon lamp (consisting of 9% UV, 43% visible light, and 48% infrared light) was used as the source of solar radiation. The source was placed 10 cm away from the reactor. The entire reaction system (source of irradiation and the reactor) was cooled using a ventilation device to avoid overheating. An injector equipped with a 0.45 nm filter was used for sampling at different time intervals. The filter was used to ensure that the collected solution was free from photocatalyst. The residual concentration of ENR in the solution was analyzed using liquid chromatograph/mass spectrometer (LC/MS, AB SCIEX 5500). A similar process was applied for ENR degradation by HSCB or H_2-TiO_2. The dosage for HSCB and H_2-TiO_2 was 20 mg and 25 mg, respectively. For the repeated MB degradation test, the process was similar to the degradation of ENR except the dark adsorption time, degradation time, and sampling intervals were 15 min, 3 h, and 5 min, respectively. The concentration of MB was analyzed using a UV−visible spectrophotometer. The photocatalysts were recycled by a simple back wash and dry process.

3. RESULTS AND DISCUSSION

3.1. Characterization. The specific surface area of HSCB, HSCB/H_2-TiO_2, and pure TiO_2 nanoparticles and their pore characteristics were investigated by N_2 adsorption−desorption isotherm (Figure S1), and the results can be found in Table S1. The BET surface area of HSCB was 43.7281 m^2/g, which provided great adsorption capacity. Due to the adherence of H_2-TiO_2, the BET surface area of HSCB/H_2-TiO_2 was larger than that of HSCB. Meanwhile, the increased average pore diameter suggests that H_2-TiO_2 was densely loaded on the HSCB surface. Compared to pure TiO_2 nanoparticles, the specific area and pore volume were decreased slightly. However, support from the biochar may provide easy separation to the composites. In addition, the biochar support has great capability for absorbing the pollutants, preventing them fromdissolving into the bulk solution, concentrating a target pollutant-rich environment at the HSCB/H_2-TiO_2

https://doi.org/10.1021/acsomega.2c00523
ACS Omega 2022, 7, 12158−12170

interface.[26] In comparison with HSCB/H_2-TiO_2, pure TiO_2 nanoparticles would allow the dissolution of pollutants. Only when the pollutants collide with TiO_2 again could the degradation be further conducted. These results may indicate that the HSCB/H_2-TiO_2 can adsorb pollutants efficiently and have excellent reusability.

The morphology of as-prepared hydrogenated SCB-derived biochar (HSCB) and HSCB/H_2-TiO_2 was recorded using SEM (Figure 1a−c,e). EDS mapping of a selected area is displayed in Figure 1d,f. As shown in Figure 1a,b, the lotus-stem-like multichannel hierarchical structure of HSCB was an ideal skeleton for the anchoring of TiO_2. Interestingly, uniformly dispersed holes (UDHs) with an average diameter of ∼0.8 μm were observed on the side walls of HSCB. They act like channels connecting the internal structure of HSCB and the external environment, allowing more efficient mass transfer. In addition, they also neutralize the effect of the decrease in surface area and the change in pore size distribution caused by blocking the pore entrances with H_2-TiO_2. Figure 1c,e shows the microstructure of the channels and the surface of HSCB/H_2-TiO_2, respectively. As shown in Figure 1c, the typical hierarchical structure remained unchanged with full coverage of H_2-TiO_2. The multichannel organic framework provided a significantly large surface area and became a good site for the anchoring of TiO_2. Uniform and dense deposition of H_2-TiO_2 can be observed on the surface of HSCB in Figure 1e. The EDS spectra (Figure 1d,f) further confirmed the universal distribution of H_2-TiO_2.

The dispersion and crystalline structure of HSCB (Figure 1g) and HSCB/H_2-TiO_2 (Figure 1h−j) were further studied by HRTEM analysis. Comparing HSCB with HSCB/H_2-TiO_2, full coverage of H_2-TiO_2 on the HSCB surface can be observed. H_2-TiO_2 particles were anchored tightly on the HSCB surface, and clear lattice fringes were observed (Figure 1i), representing the well-defined crystalline structure of H_2-TiO_2. A fringe spacing of 0.35 nm indicates the successful synthesis of anatase TiO_2.[27] Among anatase, brookite, and rutile TiO_2, anatase TiO_2 has the highest visible-light adsorption and fastest organic degradation efficiency.[28]

The XRD patterns of H_2-TiO_2 and HSCB/H_2-TiO_2 were recorded and are shown in Figure 2a. The XRD pattern of anatase TiO_2 (PDF no. 21-1272) was also recorded for reference. It can be seen that all characteristic peaks of HSCB/H_2-TiO_2 were consistent with those of anatase H_2-TiO_2. The (101) diffraction peak of HSCB/H_2-TiO_2 appeared at 2θ of 25.3°, representing an interplanar distance of 0.352 nm,[29] consistent with the TEM result. The peak intensity of HSCB/H_2-TiO_2 clearly decreased compared with H_2-TiO_2, indicating that the composition significantly affected the crystalline structure of H_2-TiO_2.

To further characterize the composite, the FTIR spectra of HSCB and HSCB/H_2-TiO_2 were recorded, as shown in Figure 2b. The absorption peaks of HSCB at 3448 and 1612 cm^{-1} can be attributed to the hydroxyl group or absorbed water (O−H stretching mode)[30] and the skeletal vibration of carbon framework,[31] respectively. The spectra of HSCB/H_2- TiO_2 showed a similar pattern; a new characteristic peak appeared at ∼620 cm^{-1}, can be attributed to the vibration of Ti−O−Ti and Ti−O−C bonds.[31] The strong signal of Ti−O−R (R = Ti or C) bonds in HSCB/H_2-TiO_2 indicated that the chemical bonds between H_2-TiO_2 particles and the HSCB surface were formed during the hydrothermal and hydrogenation process. In addition, compared to HSCB, the adsorption peak at 3448 cm^{-1} in HSCB/H_2-TiO_2 red-shifted slightly and its intensity was increased. This can be attributed to the increased hydrophilicity of surface-loaded H_2-TiO_2. According to previous studies, pure TiO_2 is less hydrophilic (contact angle 72° ± 1°) without UV irradiation,[32] which would restrict the absorption of water. In the present study, HSCB/H_2-TiO_2 exhibited increased hydrophilicity even under solar irradiation. We measured the hydrophilicity under ambient environment via contact angle tests, and the results are shown in Figure S2. HSCB and HSCB/H_2-TiO_2 had good contact with water, and their contact angles were 33.69° and 40.86°, respectively. The tendency to contact with water allowed the HSCB/H_2-TiO_2 surface to absorb more water molecules, resulting in the amplification of absorption peaks at 3448 cm^{-1}. Moreover, the decrease in contact angle could be considered as evidence that TiO_2 was excited. Accordingly, the hydrophilicity of TiO_2 would not be any different when irradiated by solar light, but it becomes more hydrophilic under UV irradiation.[32] This is because the electrons present in TiO_2 could be easily excited by UV irradiation. After the electron excitation, the holes left in the conduction band would diffuse and accumulate at the TiO_2 surface where they were captured by the reduced species (normally −OH) present in the electrolyte,[33] and the original less hydrophilic surface would be modified into a super hydrophilic surface.

XPS is a powerful technique to investigate the chemical state and environment on the surface of HSCB/H_2-TiO_2. The full-scale XPS spectra of HSCB and HSCB/H_2-TiO_2 are shown in Figure 2c. Typical Ti 2p, O 1s, and C 1s peaks could be observed in Figure 2c, confirming that TiO_2 particles were successfully deposited on the biochar.

The O 1s high-resolution XPS spectra of HSCB/H_2-TiO_2 and HSCB were deconvoluted and are shown in Figure 2d,e, respectively. Compared with HSCB, a new peak appeared at ∼532.1 eV in the HSCB/H_2-TiO_2 sample. This peak could be assigned to Ti−O[17,34−39] from the TiO_2 lattice, and it demonstrated the successful deposition of H_2-TiO_2 onto the HSCB surface, which is consistent with the TEM and FTIR results. Additionally, a slight shift could be observed in HSCB/H_2-TiO_2. The peak located at ∼530.9 eV represented the −COOH,[37] and it shifted from 530.9 to 531.4 eV. The shift was a significant signal for the change in the surface chemical environment. This change may be the result of the formation of oxygen vacancy.[38,39]

The C 1s deconvoluted XPS spectra of HSCB/H_2-TiO_2 and HSCB are shown in Figure 2f,g, respectively. In the HSCB, there are three identical peaks that can be assigned to C_n (∼284.7 eV),[17,34,36,38,40] C−OR/C−OH (∼285.6 eV), and C═O (∼287.7 eV).[38] According to the previous report, the peak representing C−OR/C−OH normally appeared at around 286.1 eV.[40] The obvious change in the peak location (286.1 to 285.6 eV) is mainly because of the formation of PFRs inside the biochar. Similar peaks can be located in HSCB/H_2-TiO_2, except the C═O peak shifted from ∼287.7 to 287.1 eV and there is a drastic drop in the concentration of C−O peak. With the load of TiO_2, Ti−O−C bonds were formed on the HSCB surface and the surface chemical environment was changed. Consequently, the shift toward lower binding energy region happened in the characteristic peak of C−OR (from 288.9 to 287.6 eV) and the concentration of C−O decreased (from 25.9% to 14.3%). The characteristic peak of Ti−C bond located at ∼281 eV was not observed. This indicated that the substitution of TiO_2

https://doi.org/10.1021/acsomega.2c00523
ACS Omega 2022, 7, 12158−12170

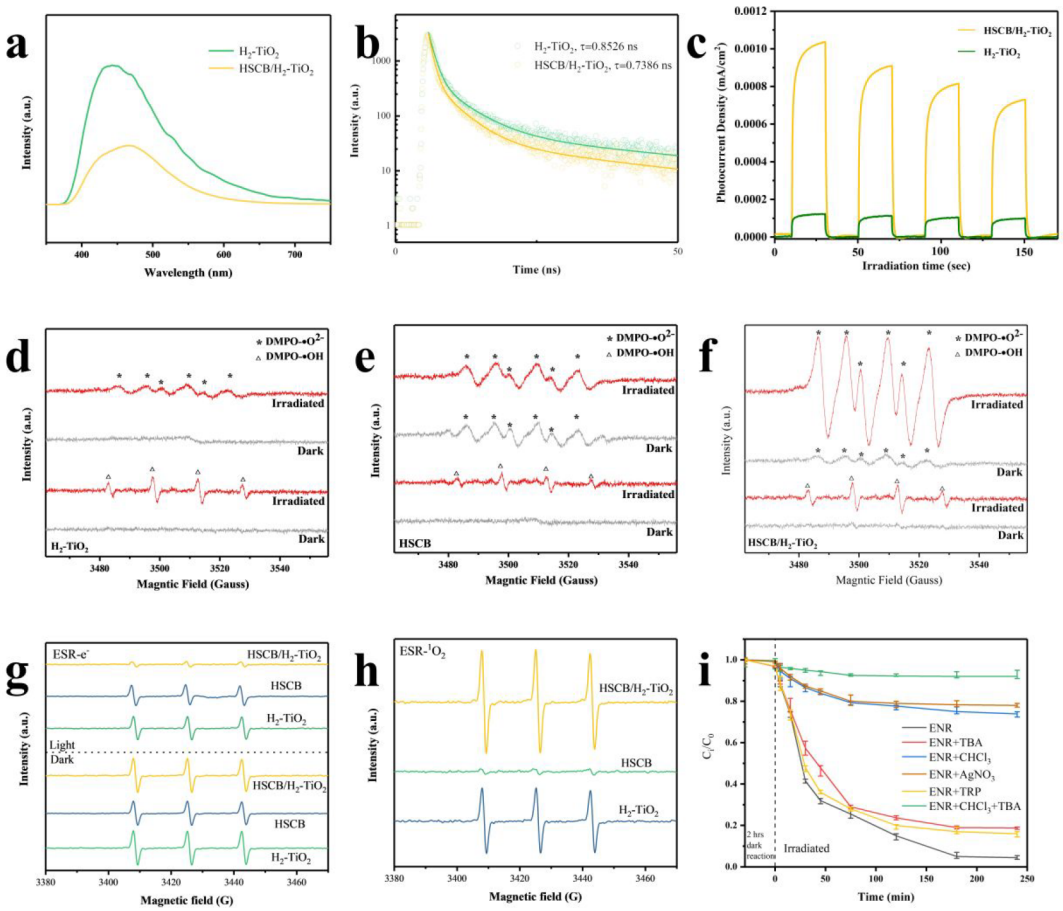

Figure 3. (a–c) Steady-state PL spectra, transient PL spectra, and current versus time (I–t) curves, respectively, for H_2-TiO_2 and HSCB/H_2-TiO_2. (d–f) EPR-DMPO radical trapping tests against (d) H_2-TiO_2, (e) HSCB, and (f) HSCB/H_2-TiO_2. (g, h) EPR-e^- and EPR-$^1O_2$ trapping results, respectively. (i) Result of ENR degradation by HSCB/H_2-TiO_2 with different scavengers for radical quenching.

lattice oxygen atom by carbon atom did not happen.[35,36,38] The discussion above is highly in accordance with the XPS O 1s results and the FT-IR spectra.

Figure 2h shows the Ti 2p XPS spectra of HSCB/H_2-TiO_2. Two typical deconvoluted peaks located at ∼458.8 eV and ∼464.5 eV corresponding to Ti^{4+} $2p_{3/2}$ and Ti^{4+} $2p_{1/2}$ could be found in both samples. Two new peaks located at ∼456.2 eV and ∼461.9 eV corresponded to the Ti^{3+} $2p_{3/2}$ and Ti^{3+} $2p_{1/2}$ orbitals, respectively.[17] The Ti^{3+} XPS signal confirmed the existence of Ti^{3+} in the composite and was also a strong evidence for the formation of oxygen vacancy in the TiO_2 lattice, because oxygen vacancies and Ti^{3+} must be present together to reach charge equilibrium.[17]

The concentration of defects has been considered as a key factor affecting the photodegradation efficiency of photocatalytic materials. During hydrogenation, defects such as Ti^{3+} and oxygen vacancies could be formed in the TiO_2 lattice and PFRs would be formed in the HSCB.[41] The PFRs would produce reactive oxygen species (ROS) when the HSCB contacted water.[24,42,43] Thus, EPR was applied to determine the number of defect species (such as Ti^{3+}, oxygen vacancies and PFRs in this case) in HSCB and HSCB/H_2-TiO_2. Compared to traditional X-ray-based techniques, EPR can be used to determine the number of unpaired electrons inside materials by recording the resonance of electrons. As shown in the EPR spectra of pure TiO_2, H_2-TiO_2, HSCB, and HSCB/H_2-TiO_2 (Figure 2i), pure TiO_2 barely displayed any signal, and H_2-TiO_2 presented clear signals owing to the hydrogenation-induced Ti^{3+} and oxygen vacancies. Both HSCB and HSCB/H_2-TiO_2 showed very strong EPR signal owing to the large amount of PFRs present in biochar[43] and the defect sites presented in H_2-TiO_2.[9] A previous study revealed that, in the absence of H_2O_2, when HSCB contacted aqueous solution, the PFRs would transfer an electron to dissolved oxygen forming $^{\bullet}O_2^-$.[42] HSCB/H_2-TiO_2 showed even stronger EPR signal compared to HSCB, which can be attributed to significantly increased defect sites in the H_2-TiO_2. The enriched defects might be introduced by the synergistic effect of hydrogenation[44] and carbothermal reduction.[17] With the help of abundant defects, more electrons can be easily excited (due to the lower energy level of defects), leading to higher production of ROS. Based on the results of XPS and EPR analysis, it can be predicted that the organic/inorganic composites will achieve a higher photodegradation efficiency than TiO_2 or HSCB.

3.2. Measurement of Photodegradation-Related Properties. The amount of excited electrons from H_2-TiO_2 was found to be critical for successful photodegradation in water. However, the excited electrons were highly inclined to recombine with holes. To increase the photodegradation efficiency, a good method is to decrease the electron–hole recombination rate. Steady-state and transient PL spectra were used to evaluate the recombination rate. It can be seen in Figure 3a,b that HSCB/H_2-TiO_2 had weaker steady-state PL

https://doi.org/10.1021/acsomega.2c00523
ACS Omega 2022, 7, 12158–12170

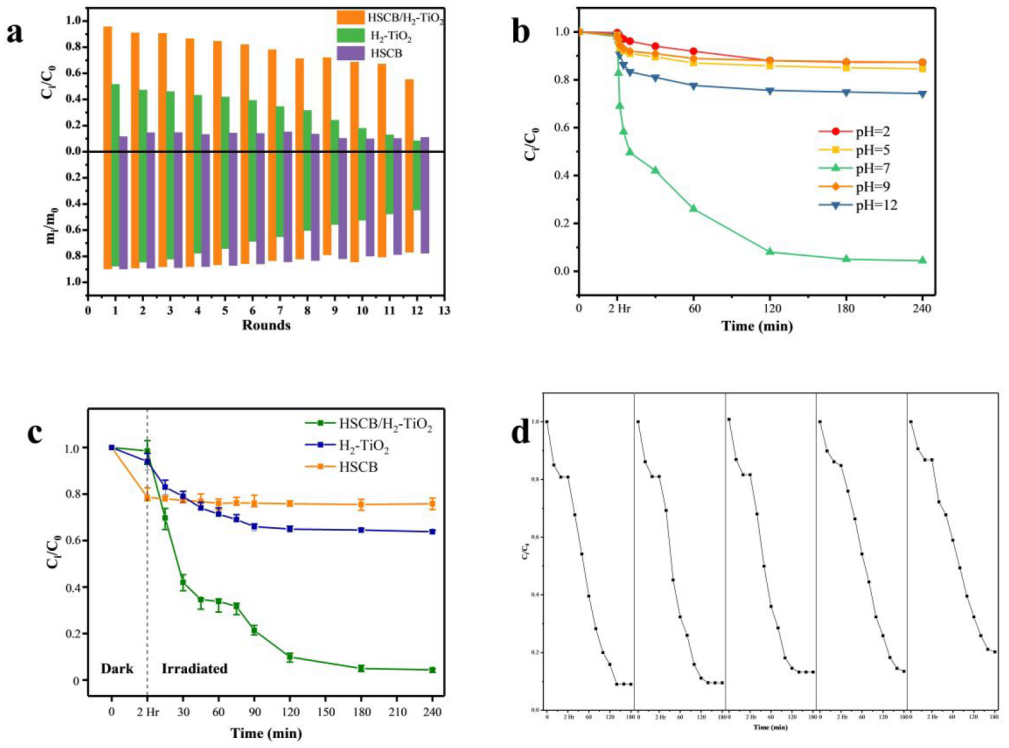

Figure 4. (a) Repeated MB degradation results: (top) MB degradation rate by different samples at the end of each round; (bottom) recovery rate of samples at the end of each round. (b) ENR degradation by HSCB/H_2-TiO_2 at different pH values. (c) Degradation efficiencies of various samples at pH = 7 for ENR. The first 2 h was reacted in dark reaction, followed by a 240 min of solar irradiation catalytic degradation. The error bar is based on the results of parallel tests. (d) Repeated ENR degradation results using HSCB/H_2-TiO_2.

intensity and shorter carrier lifetime compared to H_2-TiO_2, indicating that it has a lower electron−hole recombination rate under solar irradiation.[45] The efficient separation between electrons and holes may be explained by the numerous hydrogenation-induced defect sites. They act like electron sinks to facilitate the separation of electron−hole pairs.[46]

Measurement of transient photocurrent response is an effective method to quantify the amount of excited electrons from H_2-TiO_2. The *I*−*t* curves of H_2-TiO_2 and HSCB/H_2-TiO_2 with on−off cycles recorded under xenon lamp irradiation are shown in Figure 3c. Both as-prepared samples responding to the xenon lamp showed similar *I*−*t* patterns, demonstrating their excellent visible-light absorption. Furthermore, the photocurrent intensity of HSCB/H_2-TiO_2 was almost quintupled compared with that of H_2-TiO_2. The increase can be attributed to electrons provided by the PFRs from biochar and the excited electrons from surface loaded H_2-TiO_2. Once the electrons were excited by the incident irradiation, they were rapidly transferred to the back-contacted ITO electrode via graphitized HSCB.[47] Therefore, higher photocurrent density and more efficient production of ROS could be achieved simultaneously, and the degradation ability of the composite would be increased.

In order to determine the quantity of ROS generated in aqueous solution, EPR DMPO spin-trapping experiments with H_2-TiO_2 (Figure 3d), HSCB (Figure 3e), and HSCB/H_2-TiO_2 (Figure 3f) were performed, and the spectra of $^{\bullet}O_2^-$ and $^{\bullet}OH$ under dark conditions and light irradiation were obtained. As shown in the DMPO trapping results, without irradiation no $^{\bullet}OH$ signal was observed in all three samples and weak $^{\bullet}O_2^-$ signal can be detected in HSCB and HSCB/H_2-TiO_2. This was because the PFRs contained in the biochar can be sensitized and generate electrons when in contact with water. The as-generated electrons are then transmitted to oxygen to form $^{\bullet}O_2^-$. After 5 min of solar irradiation, typical $^{\bullet}OH$ and $^{\bullet}O_2^-$ signals could be observed in all samples. For HSCB, compared with the signals under dark conditions, the $^{\bullet}O_2^-$ signal remained almost unchanged and the $^{\bullet}OH$ signal appeared. The $^{\bullet}OH$ signal from HSCB is because the as-formed $^{\bullet}O_2^-$ can easily dismutate with H^+ to form H_2O_2, which can be photosensitized to form $^{\bullet}OH$[42] then captured by the DMPO. Moreover, the obvious $^{\bullet}OH$ and $^{\bullet}O_2^-$ signals from H_2-TiO_2 confirm that H_2-TiO_2 can be successfully excited by solar irradiation. After excitation, electrons in the valence band can jump into the conduction band and leave holes behind in the valence band. Those electrons and holes will then transport to the surface of H_2-TiO_2 to react with O_2 and H_2O, forming $^{\bullet}O_2^-$ and $^{\bullet}OH$, respectively. Based on the even stronger $^{\bullet}O_2^-$ and $^{\bullet}OH$ signals from HSCB/H_2-TiO_2, we can predict that HSCB/H_2-TiO_2 generates more ROS in water compared with other samples and excellent degradation performance can be predicted.

Besides $^{\bullet}OH$ and $^{\bullet}O_2^-$, we also investigated other active oxidation species by ESR, such as $^1O_2$ and electrons. TEMP and TEMPO were used as spin trapping agents for $^1O_2$ and e^-, respectively. The ESR spin trapping spectra of e^- and $^1O_2$ are shown in Figure 3g,h, respectively. It can be seen from ESR-e^- spectra that H_2-TiO_2 did not generate any e^- without irradiation. Even under dark conditions, the ESR-e^- signal of HSCB and HSCB/H_2-TiO_2 decreased, revealing that they can generated electrons without visible irradiation, which was inconsistent with the ESR-$^{\bullet}O_2^-$ results. When visible irradiation was applied, significant decrease in the intensity of the ESR-$^{\bullet}O_2^-$ signal could be observed in all three samples,

https://doi.org/10.1021/acsomega.2c00523
ACS Omega 2022, 7, 12158−12170

Table 1. Photocatalytic Degradation Efficiencies of Various Photocatalysts for ENR

photocatalyst	light	cat. dosage (g L^{-1})	ENR concn (mg L^{-1})	degradation efficiency	ref
Ti-KBC	visible light (15 W)	2.5	100	58.97% in 60 min	50
GaOOH/$ZnBiTaO_5$	mercury lamp (500 W)	1	10	58.27% in 60 min	51
P_2−Mn_3O_4	xenon lamp (500 W)	0.1	*a*	72.3% in 10 min (with the addition of PMS)	52
BN/$BiPO_4$	UV light (250 W)	3.33	10	91.5% in 2 h	53
HSCB/H_2-TiO_2	xenon lamp (250 W)	0.1	3.6	95.6% in 180 min	this work

[a]Not reported.

indicating that a huge amount of electrons were generated. Proposed by other researchers, $^1O_2$ can be generated via oxidation of $^{\bullet}O_2^-$ (eq 1).[48,49] Thus, the ESR-$^1O_2$ spectra could be used as proof of the simultaneous existence of $^{\bullet}OH$ and $^{\bullet}O_2^-$. The results of ESR-$^1O_2$ demonstrated that HSCB cannot generate $^{\bullet}OH$ even with irradiation applied.

$$^{\bullet}O_2^- + {}^{\bullet}OH \rightarrow {}^1O_2 + OH^- \quad (1)$$

Radical quenching tests were conducted to estimate the contribution from different ROS, and the results are shown in Figure 3i. HSCB/H_2-TiO_2 was used as photocatalyst. $AgNO_3$, Trp, $CHCl_3$, and TBA were used as scavengers for e^-, $^1O_2$, $^{\bullet}O_2^-$, and $^{\bullet}OH^-$, respectively. It can be seen that after 2 h dark reaction, the concentration of ENR did not decrease in the samples without $^{\bullet}O_2^-$. The concentration slightly dropped in the samples in which $^{\bullet}O_2^-$ was not quenched. This indicates that biochar can generate $^{\bullet}O_2^-$ without any irradiation. The result is highly in accordance with the analysis of EPR spin trapping results. After solar irradiation was applied, ENR concentration drops quickly in the samples in which $^{\bullet}O_2^-$ was not quenched. The degradation reached equilibrium in 180 min, and the final degradation rate could reach 81.2% (ENR + TBA) and 95.6% (ENR). In contrast, in the samples without $^{\bullet}O_2^-$, the degradation rates of ENR were greatly inhibited and its concentration hardly decreased after 120 min. The final degradation rates were only 26.1% (ENR + $CHCl_3$) and 8% (ENR + TBA + $CHCl_3$). From the quenching results, it can be concluded that $^{\bullet}O_2^-$ contributes to the ENR degradation more than $^{\bullet}OH^-$.

3.3. Measurement of Durability of the Photocatalyst.

MB is a commonly used organic dye and chemical indicator. The solar-irradiation degradation of MB by HSCB/H_2-TiO_2 was recorded to simulate the degradation of organic dyes, and its degradation by HSCB and H_2-TiO_2 particles was used for comparison. The final degradation rate for each round is shown in Figure 4a. HSCB/H_2-TiO_2 can degrade MB effectively under solar irradiation. At the end of first round, about 95.4% of MB was removed by HSCB/H_2-TiO_2, while the HSCB and H_2-TiO_2 only removed 12% and 49% of MB. After 12 rounds of repeated degradation, HSCB/H_2-TiO_2 could still degrade ∼55.1% of MB, while less than 9% and 11% MB could be degraded by H_2-TiO_2 and HSCB, respectively. The recovery rate of all photocatalysts at the end of each round is also recorded in Figure 4a. The weight of recovered HSCB/H_2-TiO_2 decreased smoothly and gradually. The final weight of HSCB/H_2-TiO_2 after 12 rounds remained around 84% of the initial weight. The HSCB underwent 15% weight loss, retaining 84.8% of its initial weight. For comparison, the weight loss of H_2-TiO_2 particles was as high as 51%. The small particle size of H_2-TiO_2 might be responsible for the unexpected loss. It is highly possible that small particles were stuck on the filter paper during separation. This is strong evidence for the superior durability of composites and the great separation ability of HSCB/H_2-TiO_2. We attributed the high durability of our composite to the mild synchronous hydrogenation. After the deposition of the Ti precursor, the mild hydrogenation facilitated further growth of TiO_2 on the surface of cellulose. Strong bonding between the biochar and H_2-TiO_2 reduced the leaching of surface-loaded catalysts. On the other hand, low hydrogenation temperature allowed the biochar to maintain its external shape almost undamaged, which was beneficial for easy separation. Moreover, during repeated tests, the mass loss of HSCB/H_2-TiO_2 was acceptable. It was indicated that the template had excellent strength. We compared the HSCB/H_2-TiO_2 with previous reports. The results are listed in Table 1. The as-synthesized photocatalyst showed superior photocatalytic performance in ENR degradation.

3.4. ENR Degradation Test and Possible Mechanism.

The effect of different solution pH on the ENR degradation by HSCB/H_2-TiO_2 was monitored, and the results are showed in Figure 4b. It can be seen that the most ENR could be degraded in neutral solution. The effect of different pH value could be explained because in the acidic environment, the surface-loaded TiO_2 and ENR were both positively charged while they were both negatively charged in the alkaline environment. Therefore, when the solution pH deviated from neutral, electrostatic repulsion would occur between the catalyst and the targeted antibiotic and prevented them from contacting, which would drastically impede the ENR degradation efficiency.

Figure 4c displayed the results of the degradation of ENR using HSCB/H_2-TiO_2, HSCB, and H_2-TiO_2. As can be seen, the adsorption percentage of H_2-TiO_2 and HSCB/H_2-TiO_2 was 6% and 1.6%, respectively. The adsorption percentages were in accordance with their specific surface area. For HSCB, the ENR removal percentage was 20.5% during the 2 h dark reaction. HSCB exhibited the lowest specific surface area among HSCB, H_2-TiO_2, and HSCB/H_2-TiO_2. However, based on the results of active oxidation species trapping ESR spectra, HSCB generated e^- even under dark conditions. Therefore, the ENR removal was not only contributed by the physical adsorption but also the oxidation by the active oxidation species in the water. During the following 240 min irradiation, the concentration barely reduced. It can be concluded that the degradation reached equilibrium after the 2-h dark reaction. For the H_2-TiO_2 and HSCB/H_2-TiO_2 samples, when the simulated irradiation was applied, the concentration of ENR dropped drastically in the first 15 min for both samples. This was because the ENR underwent self-sensitized photolysis and light-excited electron direct photolysis. According to previous research,[54] solar irradiation can be absorbed by ENR, and the exposure to irradiation can destroy ENR's resistance to radical degradation. From 15 to 30 min, the ENR continued to be drastically degraded by HSCB/H_2-TiO_2, while the rate of

https://doi.org/10.1021/acsomega.2c00523
ACS Omega 2022, 7, 12158−12170

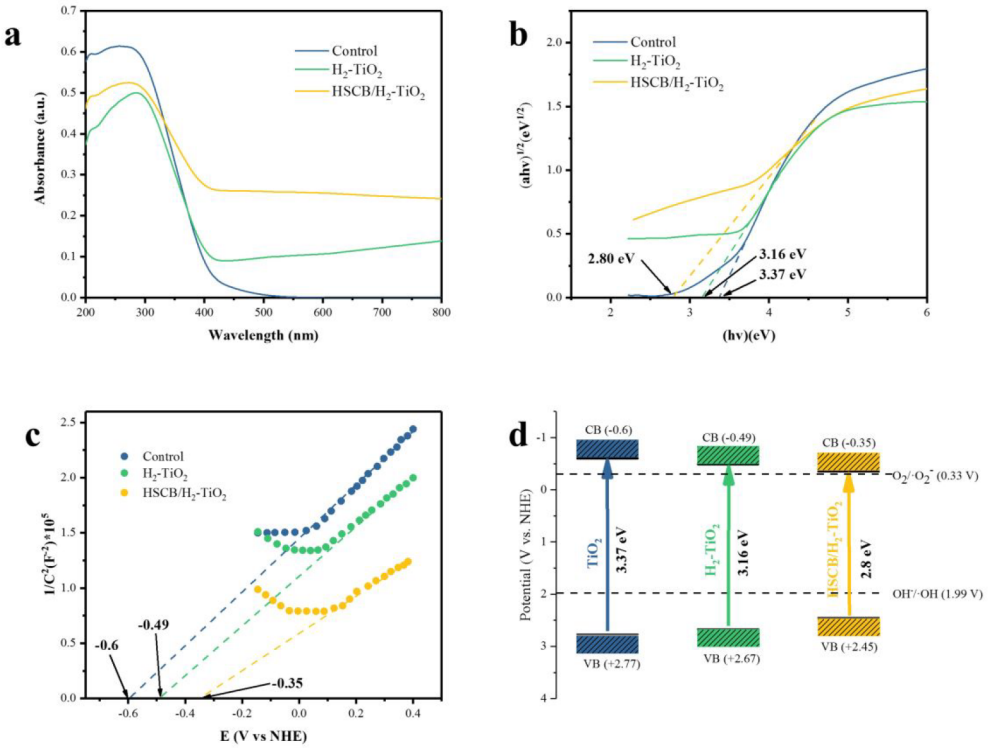

Figure 5. (a) UV−vis/DRS spectra of H_2-TiO_2 and HSCB/H_2-TiO_2. Data for TiO_2 was used as control group. (b, c) Tauc plot and Mott−Schottky plot for the samples. (d) Scheme of the energy band structures of as-prepared samples.

degradation of ENR by H_2-TiO_2 decreased. Based on the discussion of the excess amount of electrons provided by HSCB and the improved hydrophilicity of HSCB/H_2-TiO_2, more electrons and holes were created and transferred to the surface of the composites, contacting with surface-absorbed ENR molecules and facilitating the degradation. After 30 min, the rate of degradation of ENR by HSCB/H_2-TiO_2 started to decrease because ENR contains carbonyl, C−F bonds, and piperazinyl, which are very hard to break. Self-sensitized photolysis and electron direct photolysis were not strong enough to break them. However, in the heterogeneous photocatalytic system, strongly oxidizing $^{\bullet}O^{2-}$ and $^{\bullet}OH$ can be generated, and under their attacks, decarboxylation, defluorination, or piperazinyl N4-dealkylation occurred effectively.[55] Eventually, hydroxyl and superoxide radical oxidation will degrade ENR into CO_2, H_2O, F^-, and NO_3^-. The whole degradation test lasted for 4 h, and it reached equilibrium in 180 min. The equilibrium degradation efficiency reached as high as 95.6%. The photostability of HSCB/H_2-TiO_2 was tested by five rounds of repeated ENR degradation. The results in Figure 4d demonstrated that our catalysts had great photostability. After 5 rounds of repeated tests, the degradation efficiency could still reach 77%. In addition, we measured the total organic carbon (TOC) removal efficiency using HSCB/H_2-TiO_2 to further explore its mineralization capability. The results are shown in Figure S3. It could be seen that around 77% of TOC could be removed in 240 min under visible irradiation, demonstrating the excellent mineralization capability of HSCB/H_2-TiO_2.

H_2-TiO_2 and HSCB/H_2-TiO_2 were characterized by UV−vis/diffuse reflection spectroscopy (DRS0 (Figure 5a) and with an electrochemical workstation. Data on TiO_2 was also collected as control group. Their bandgap (E_g) and conductive band edge (E_{CB}) were estimated via Tauc plots (Figure 5b) and Mott−Schottky plots (Figure 5c), respectively. The valence band edge (E_{VB}) of samples was calculated by combining the value of E_{CB} with E_g, and the results are shown in Figure 5d, together with the potentials of $O_2/^{\bullet}O_2^-$ (−0.33 V) and $OH^-/^{\bullet}OH$ (3.2 V). It can be seen from Figure 5a that the light absorption range of TiO_2 was from 200 to 500 nm and those of H_2-TiO_2 and HSCB/H_2-TiO_2 were extended to 800 nm. Their absorption edges were estimated to be 420 nm (TiO_2), 445 nm (H_2-TiO_2), and 560 nm (HSCB/H_2-TiO_2), and the corresponding E_g values, estimated using Tauc plots,[56] were 3.37 eV (TiO_2), 3.16 eV (H_2-TiO_2), and 2.8 eV (HSCB/H_2-TiO_2). The addition of HSCB improved the light absorption edge and narrowed the bandgap width, enhancing the light utilization capacity of catalysts.

From the Mott−Schottky plots, it can be seen that the samples had positive slopes, implying they all are n-type semiconductors. The flat band edges of samples were estimated to be −0.6 V (TiO_2), −0.49 V (H_2-TiO_2), and −0.35 V (HSCB/H_2-TiO_2) vs Ag/AgCl. According to previous researchers, the flat band edge of an n-type semiconductor is about 0.2 V more positive than its $E_{CB.}$ Therefore, the E_{CB} values were estimated to be −0.4 V (TiO_2), −0.29 V (H_2-TiO_2), and −0.15 V (HSCB/H_2-TiO_2) vs Ag/AgCl or −0.6 V (TiO_2), −0.49 V (H_2-TiO_2), and −0.35 V (HSCB/H_2-TiO_2) vs NHE. The results showed that HSCB/H_2-TiO_2 had a less negative VB level than that of H_2-TiO_2, which revealed that the reduction ability of HSCB/H_2-TiO_2 was slightly lower. Nevertheless, from Figure 5d, the VB level of HSCB/H_2-TiO_2 was more negative than the redox potential of $O_2/^{\bullet}O_2^-$ (−0.33 V), so the catalyst still had the ability to reduce O_2 to yield $^{\bullet}O_2$. Based on the E_g and E_{CB} results, the E_{VB} can be calculated to be 2.77 V (TiO_2), 2.67 V (H_2-TiO_2), and 2.45 V (HSCB/H_2-TiO_2) vs NHE. The CB level of HSCB/H_2-TiO_2 was more positive than the redox potential of $OH^-/^{\bullet}OH$ (3.2

https://doi.org/10.1021/acsomega.2c00523
ACS Omega 2022, 7, 12158−12170

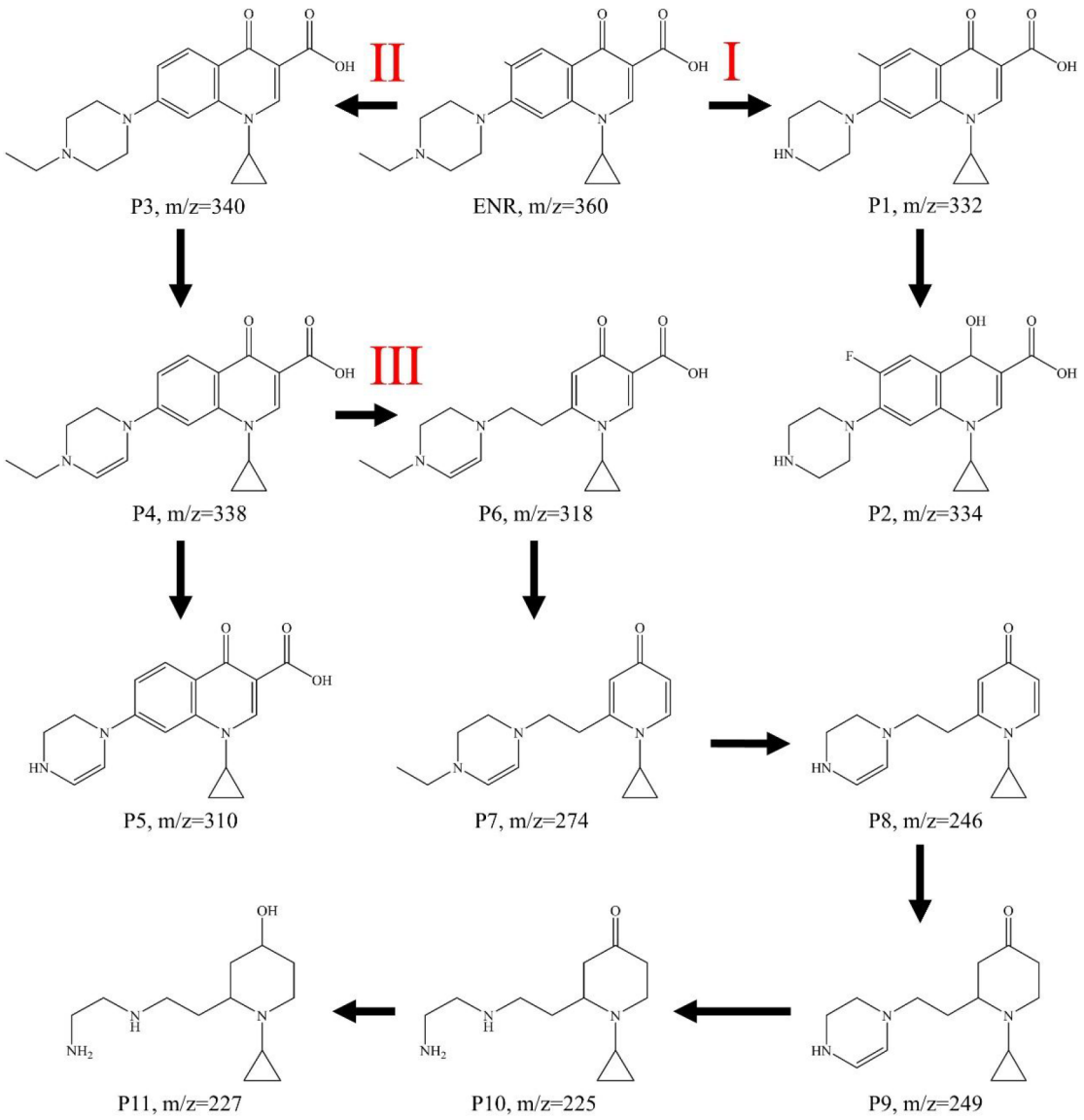

Figure 6. Possible ENR degradation pathways catalyzed by HSCB/H_2-TiO_2 under solar irradiation.

V), which revealed that $^{\bullet}OH$ radicals could be successfully produced by oxidized OH^- ion or H_2O despite the oxidation ability of HSCB/H_2-TiO_2 being weaker than that of H_2-TiO_2.

Based on the above results and discussions, a possible photocatalytic mechanism can be proposed. The one-pot hydrogenation generated abundant PFRs in the biochar support and plentiful defect sites in the surface-loaded H_2-TiO_2 simultaneously. When the catalyst contacts water, the PFRs in the biochar would be sensitized and electrons would be transferred from the PFRs to the surface of the photocatalyst. In addition, hydrogenation can effectively narrow the bandgap width of TiO_2 (from 3.37 to 3.16 eV), allowing irradiation with longer wavelength to be utilized by the photocatalysts. With the addition of sugarcane biochar, the bandgap was further narrowed to 2.8 eV. Furthermore, the addition of the biochar skeleton not only increased the separation efficiency of electron−hole pairs but also provided additional electrons to further increase the photodegradation efficiency. When simulated solar irradiation was applied, the defect-induced lower energy band allowed more electrons to be excited from the valence band of H_2-TiO_2. The defects also acted as electron sinks to prevent the electrons from recombining with the holes. With the synergetic help of biochar and H_2-TiO_2, excess electrons accumulated on the surface of the photocatalyst, reacting with O_2 to form excess $^{\bullet}O^{2-}$, leading to high degradation efficiency against ENR.

3.5. Photocatalytic Degradation Pathways of ENR.

Eleven intermediates of ENR degradation were identified by LC-MS, and detailed information about them can be found in Table S2, and the mass spectra of intermediates are provided in Figure S4. According to the dominant ROS in the heterogeneous photodegradation system and the intermediates, three possible degradation pathways were proposed in Figure 6. The first pathway was caused by the direct photolysis by irradiation and the attack by $^{\bullet}O_2^-$. P1 was produced via de-ethylation with the attack of $^{\bullet}O_2^-$ and then was transformed into P2 via photolysis. For the second pathway, ENR was direct attacked by electrons and P3 was produced via defluorination. The piperazinyl of P3 can be continuously attacked by $^{\bullet}O_2^-$ to form P4 and P5. In the degradation of ENR, $^{\bullet}O_2^-$ and $^{\bullet}OH$ mainly attack piperazinyl[57] and quinolone,[57,58] respectively. Thus, the third pathway of ENR

https://doi.org/10.1021/acsomega.2c00523
ACS Omega 2022, 7, 12158−12170

degradation was caused by oxidation via $^{\bullet}OH$. P6 was produced through the breaking of the quinolone ring from P4. Then P6 went through decarboxylation to produce P7. P7 was continuously degraded by the synergetic attack of $^{\bullet}O_2^-$ and $^{\bullet}OH$ to produce intermediates P8−P11.

4. CONCLUSION

In summary, highly durable HSCB/H_2-TiO_2 composites capable of excellent solar-driven degradation of ENR were successfully synthesized via a facile one-pot hydrogenation for the first time. The mild hydrogenation process preserved the lotus-stem-like multichannel skeletal structure of SCB, which allowed more sites for the composites to contact water and irradiation. Characterizations revealed that H_2-TiO_2 particles were well dispersed on the surface of biochar and strongly connected with the support. Twelve rounds of repeated degradation tests were conducted, and the highly durable HSCB/H_2-TiO_2 could still degrade ∼55.1% of simulated pollutant with well-controlled mass loss. EPR DMPO trapping results and radical trapping tests demonstrated the large amount of $^{\bullet}O_2^-$ in the heterogeneous photodegradation system and the major contribution of $^{\bullet}O_2^-$ in efficient ENR degradation. Solid state EPR demonstrated the existence of PFRs in the biochar, which were the main reason for the excess amount of $^{\bullet}O_2^-$. Decreased electron−hole recombination rate of composites was determined by PL spectra, and increased transient photocurrent indicated that more photoexcited electrons were generated. Combined with the synergetic contributions from HSCB and H_2-TiO_2, efficient ENR degradation was achieved: 95.6% of ENR could be removed by HSCB/H_2-TiO_2 in 180 min. Moreover, possible photodegradation pathways of ENR were proposed based on the identified intermediates. Therefore, the highly durable HSCB/H_2-TiO_2 composites not only expand the industrial application of TiO_2 but also provide new choices for the environmental and high-value application of sugarcane bagasse.

■ ASSOCIATED CONTENT

Supporting Information

The Supporting Information is available free of charge at https://pubs.acs.org/doi/10.1021/acsomega.2c00523.

Specific area of HSCB, HSCB/H_2-TiO_2, and pure TiO_2 nanoparticles and their pore characteristics, N_2 adsorption/desorption curves and pore size distribution of HSCB, H_2-TiO_2 and HSCB/H_2-TiO_2, contact angle test result for HSCB and HSCB/H_2-TiO_2, TOC removal efficiency by HSCB/H_2-TiO_2, and mass spectra of the intermediates of ENR degradation (PDF)

■ AUTHOR INFORMATION

Corresponding Authors

Wenyu Huang − *School of Resources, Environment and Materirals, Guangxi University, Nanning, Guangxi 530000, China*; Email: huangwenyu@gxu.edu.cn

Shuangfei Wang − *Department of Light Industry and Food Engineering, Guangxi University, Nanning, Guangxi 530000, China*; Email: wangsf@gxu.edu.cn

Authors

Ji Shi − *Department of Light Industry and Food Engineering, Guangxi University, Nanning, Guangxi 530000, China*; orcid.org/0000-0002-5743-0330

Hongxiang Zhu − *Department of Light Industry and Food Engineering, Guangxi University, Nanning, Guangxi 530000, China*

Jianhua Xiong − *School of Resources, Environment and Materirals, Guangxi University, Nanning, Guangxi 530000, China*

Huiting Bei − *Department of Civil Engineering, Guangxi Polytechnic of Construction, Nanning, Guangxi 530000, China*

Complete contact information is available at: https://pubs.acs.org/10.1021/acsomega.2c00523

Notes

The authors declare no competing financial interest.

■ ACKNOWLEDGMENTS

This work was supported by the National Natural Science Foundation of China (No. 21367003), the Scientific Research and Technology Development Program of Guangxi (No. AA17202032), and the Open Fund of Guangxi Key Laboratory of Clean Pulp & Papermaking and Pollution Control (KF201724).

■ REFERENCES

(1) Brusseau, M. L.; Ramirez-Andreotta, M.; Pepper, I. L.; Maximillian, J. Environmental Impacts on Human Health and Well-Being. In *Environmental and Pollution Science*, 3rd ed.; Brusseau, M. L., Pepper, I. L., Gerba, C. P., Eds.; Academic Press: 2019; Chapter 26, pp 477−499.

(2) Wang, C.; Yin, L.; Xu, Z.; Niu, J.; Hou, L.-A. Electrochemical degradation of enrofloxacin by lead dioxide anode: Kinetics, mechanism and toxicity evaluation. *Chem. Eng. J.* **2017**, *326*, 911−920.

(3) Guo, H.; Ke, T.; Gao, N.; Liu, Y.; Cheng, X. Enhanced degradation of aqueous norfloxacin and enrofloxacin by UV-activated persulfate: Kinetics, pathways and deactivation. *Chem. Eng. J.* **2017**, *316*, 471−480.

(4) Krasucka, P.; Pan, B.; Sik Ok, Y.; Mohan, D.; Sarkar, B.; Oleszczuk, P. Engineered biochar − A sustainable solution for the removal of antibiotics from water. *Chem. Eng. J.* **2021**, *405*, 126926.

(5) Wu, S.; Hu, Y. H. A comprehensive review on catalysts for electrocatalytic and photoelectrocatalytic degradation of antibiotics. *Chem. Eng. J.* **2021**, *409*, 127739.

(6) Batchu, S. R.; Panditi, V. R.; O'Shea, K. E.; Gardinali, P. R. Photodegradation of antibiotics under simulated solar radiation: Implications for their environmental fate. *Sci. Total Environ.* **2014**, *470−471*, 299−310.

(7) Jiang, C.; Ji, Y.; Shi, Y.; Chen, J.; Cai, T. Sulfate radical-based oxidation of fluoroquinolone antibiotics: Kinetics, mechanisms and effects of natural water matrices. *Water Res.* **2016**, *106*, 507−517.

(8) Yan, L.; Kong, L.; Qu, Z.; Li, L.; Shen, G. Magnetic Biochar Decorated with ZnS Nanocrytals for Pb (II) Removal. *ACS Sustain. Chem. Eng.* **2015**, *3* (1), 125−132.

(9) Shi, J.; Huang, W.; Zhu, H.; Xiong, J.; Bei, H.; Wei, X.; Wang, S. Modified TiO2 particles for heterogeneous photocatalysis under solar irradiation. *Mater. Lett.* **2020**, *279*, 128472.

(10) O'Regan, B.; Grätzel, M. A low-cost, high-efficiency solar cell based on dye-sensitized colloidal TiO2 films. *Nature* **1991**, *353* (6346), 737−740.

(11) Asahi, R.; Morikawa, T.; Ohwaki, T.; Aoki, K.; Taga, Y. Visible-Light Photocatalysis in Nitrogen-Doped Titanium Oxides. *Science* **2001**, *293* (5528), 269.

(12) Tan, X.-f.; Liu, Y.-g.; Gu, Y.-l.; Xu, Y.; Zeng, G.-m.; Hu, X.-j.; Liu, S.-b.; Wang, X.; Liu, S.-m.; Li, J. Biochar-based nano-composites for the decontamination of wastewater: A review. *Bioresour. Technol.* **2016**, *212*, 318−333.

(13) Chen, Y.; Wang, Y.; Fang, J.; Dai, B.; Kou, J.; Lu, C.; Zhao, Y. Design of a ZnO/Poly(vinylidene fluoride) inverse opal film for photon localization-assisted full solar spectrum photocatalysis. *Chin. J. Catal* **2021**, *42* (1), 184−192.
(14) Han, B.; Wei, W.; Chang, L.; Cheng, P.; Hu, Y. H. Efficient Visible Light Photocatalytic CO2 Reforming of CH4. *ACS Catal.* **2016**, *6* (2), 494−497.
(15) Ren, Z.; Liu, X.; Zhuge, Z.; Gong, Y.; Sun, C. Q. MoSe2/ZnO/ZnSe hybrids for efficient Cr(VI) reduction under visible light irradiation. *Chin. J. Catal* **2020**, *41* (1), 180−187.
(16) Han, B.; Wei, W.; Li, M.; Sun, K.; Hu, Y. H. A thermo-photo hybrid process for steam reforming of methane: highly efficient visible light photocatalysis. *Chem. Commun.* **2019**, *55* (54), 7816−7819.
(17) Tang, J.; Liu, Y.; Hu, Y.; Lv, G.; Yang, C.; Yang, G. Carbothermal Reduction Induced Ti3+ Self-Doped TiO2/GQD Nanohybrids for High-Performance Visible Light Photocatalysis. *Chem.—Eur. J.* **2018**, *24* (17), 4390−4398.
(18) Li, Y.; Cao, L.; Li, L.; Yang, C. In situ growing directional spindle TiO 2 nanocrystals on cellulose fibers for enhanced Pb 2+ adsorption from water. *J. Hazard. Mater.* **2015**, *289*, 140−148.
(19) Lisowski, P.; Colmenares, J. C.; Mašek, O.; Lisowski, W.; Lisovytskiy, D.; Kamińska, A.; Łomot, D. Dual Functionality of TiO2/Biochar Hybrid Materials: Photocatalytic Phenol Degradation in the Liquid Phase and Selective Oxidation of Methanol in the Gas Phase. *ACS Sustain. Chem. Eng.* **2017**, *5* (7), 6274−6287.
(20) Adams, M. M.; Benjamin, T. J.; Emery, N. C.; Brouder, S. J.; Gibson, K. D. The Effect of Biochar on Native and Invasive Prairie Plant Species. *Invas. Plant Sci. Manage.* **2013**, *6* (2), 197−207.
(21) Jiang, J.; Zhang, L.; Wang, X.; Holm, N.; Rajagopalan, K.; Chen, F.; Ma, S. Highly ordered macroporous woody biochar with ultra-high carbon content as supercapacitor electrodes. *Electrochim. Acta* **2013**, *113*, 481−489.
(22) Leary, R.; Westwood, A. Carbonaceous nanomaterials for the enhancement of TiO2 photocatalysis. *Carbon* **2011**, *49* (3), 741−772.
(23) Liu, W.-J.; Jiang, H.; Yu, H.-Q. Development of Biochar-Based Functional Materials: Toward a Sustainable Platform Carbon Material. *Chem. Rev.* **2015**, *115* (22), 12251−12285.
(24) Huang, D.; Luo, H.; Zhang, C.; Zeng, G.; Lai, C.; Cheng, M.; Wang, R.; Deng, R.; Xue, W.; Gong, X.; Guo, X.; Li, T. Nonnegligible role of biomass types and its compositions on the formation of persistent free radicals in biochar: Insight into the influences on Fenton-like process. *Chem. Eng. J.* **2019**, *361*, 353−363.
(25) Pandey, A.; Soccol, C. R.; Nigam, P.; Soccol, V. T. Biotechnological potential of agro-industrial residues. I: sugarcane bagasse. *Bioresour. Technol.* **2000**, *74* (1), 69−80.
(26) Torimoto, T.; Ito, S.; Kuwabata, S.; Yoneyama, H. Effects of Adsorbents Used as Supports for Titanium Dioxide Loading on Photocatalytic Degradation of Propyzamide. *Environ. Sci. Technol.* **1996**, *30* (4), 1275−1281.
(27) Zhou, L.; Cai, M.; Zhang, X.; Cui, N.; Chen, G.; Zou, G.-y. In-situ nitrogen-doped black TiO2 with enhanced visible-light-driven photocatalytic inactivation of Microcystis aeruginosa cells: Synthesization, performance and mechanism. *Appl. Catal., B* **2020**, *272*, 119019.
(28) Hanaor, D. A. H.; Sorrell, C. C. Review of the anatase to rutile phase transformation. *J. Mater. Sci.* **2011**, *46* (4), 855−874.
(29) Pan, J.; Dong, Z.; Wang, B.; Jiang, Z.; Zhao, C.; Wang, J.; Song, C.; Zheng, Y.; Li, C. The enhancement of photocatalytic hydrogen production via Ti3+ self-doping black TiO2/g-C3N4 hollow core-shell nano-heterojunction. *Appl. Catal., B* **2019**, *242*, 92−99.
(30) Meldrum, B. J.; Rochester, C. H. Infrared spectra of carbonaceous chars under carbonization and oxidation conditions. *Fuel* **1991**, *70* (1), 57−63.
(31) Zhang, H.; Lv, X.; Li, Y.; Wang, Y.; Li, J. P25-Graphene Composite as a High Performance Photocatalyst. *ACS Nano* **2010**, *4* (1), 380−386.
(32) Wang, R.; Hashimoto, K.; Fujishima, A.; Chikuni, M.; Kojima, E.; Kitamura, A.; Shimohigoshi, M.; Watanabe, T. Light-induced amphiphilic surfaces. *Nature* **1997**, *388* (6641), 431−432.
(33) Wang, R.; Hashimoto, K.; Fujishima, A.; Chikuni, M.; Kojima, E.; Kitamura, A.; Shimohigoshi, M.; Watanabe, T. Photogeneration of Highly Amphiphilic TiO2 Surfaces. *Adv. Mater.* **1998**, *10* (2), 135−138.
(34) Zhong, J.; Chen, F.; Zhang, J. Carbon-Deposited TiO2: Synthesis, Characterization, and Visible Photocatalytic Performance. *J. Phys. Chem. C* **2010**, *114* (2), 933−939.
(35) Jia, G.; Wang, Y.; Cui, X.; Zheng, W. Highly Carbon-Doped TiO2 Derived from MXene Boosting the Photocatalytic Hydrogen Evolution. *ACS Sustain. Chem. Eng.* **2018**, *6* (10), 13480−13486.
(36) Yu, S.; Zhong, Y.-Q.; Yu, B.-Q.; Cai, S.-Y.; Wu, L.-Z.; Zhou, Y. Graphene quantum dots to enhance the photocatalytic hydrogen evolution efficiency of anatase TiO2 with exposed {001} facet. *Phys. Chem. Chem. Phys.* **2016**, *18* (30), 20338−20344.
(37) Parayil, S. K.; Kibombo, H. S.; Wu, C.-M.; Peng, R.; Baltrusaitis, J.; Koodali, R. T. Enhanced photocatalytic water splitting activity of carbon-modified TiO2 composite materials synthesized by a green synthetic approach. *Int. J. Hydrogen Energy* **2012**, *37* (10), 8257−8267.
(38) Liu, J.; Han, L.; An, N.; Xing, L.; Ma, H.; Cheng, L.; Yang, J.; Zhang, Q. Enhanced visible-light photocatalytic activity of carbonate-doped anatase TiO2 based on the electron-withdrawing bidentate carboxylate linkage. *Appl. Catal., B* **2017**, *202*, 642−652.
(39) Xing, M.; Fang, W.; Nasir, M.; Ma, Y.; Zhang, J.; Anpo, M. Self-doped Ti3+-enhanced TiO2 nanoparticles with a high-performance photocatalysis. *J. Catal.* **2013**, *297*, 236−243.
(40) Liu, R.; Dai, L.; Si, C.-L. Mussel-Inspired Cellulose-Based Nanocomposite Fibers for Adsorption and Photocatalytic Degradation. *ACS Sustain. Chem. Eng.* **2018**, *6* (11), 15756−15763.
(41) Tao, W.; Duan, W.; Liu, C.; Zhu, D.; Si, X.; Zhu, R.; Oleszczuk, P.; Pan, B. Formation of persistent free radicals in biochar derived from rice straw based on a detailed analysis of pyrolysis kinetics. *Sci. Total Environ.* **2020**, *715*, 136575.
(42) Liao, S.; Pan, B.; Li, H.; Zhang, D.; Xing, B. Detecting Free Radicals in Biochars and Determining Their Ability to Inhibit the Germination and Growth of Corn, Wheat and Rice Seedlings. *Environ. Sci. Technol.* **2014**, *48* (15), 8581−8587.
(43) Fang, G.; Gao, J.; Liu, C.; Dionysiou, D. D.; Wang, Y.; Zhou, D. Key Role of Persistent Free Radicals in Hydrogen Peroxide Activation by Biochar: Implications to Organic Contaminant Degradation. *Environ. Sci. Technol.* **2014**, *48* (3), 1902−1910.
(44) Chen, X.; Liu, L.; Yu, P. Y.; Mao, S. S. Increasing Solar Absorption for Photocatalysis with Black Hydrogenated Titanium Dioxide Nanocrystals. *Science* **2011**, *331* (6018), 746.
(45) Lu, Y.; Ou, X.; Wang, W.; Fan, J.; Lv, K. Fabrication of TiO2 nanofiber assembly from nanosheets (TiO2-NFs-NSs) by electrospinning-hydrothermal method for improved photoreactivity. *Chin. J. Catal* **2020**, *41* (1), 209−218.
(46) Wang, P.; Yin, G.; Bi, Q.; Huang, X.; Du, X.; Zhao, W.; Huang, F. Efficient Photocatalytic Reduction of CO2 Using Carbon-Doped Amorphous Titanium Oxide. *ChemCatChem.* **2018**, *10* (17), 3854−3861.
(47) Zhu, P.; Yin, X.; Gao, X.; Dong, G.; Xu, J.; Wang, C. Enhanced photocatalytic NO removal and toxic NO2 production inhibition over ZIF-8-derived ZnO nanoparticles with controllable amount of oxygen vacancies. *Chin. J. Catal* **2021**, *42* (1), 175−183.
(48) Wang, H.; Li, X.; Zhao, X.; Li, C.; Song, X.; Zhang, P.; Huo, P.; Li, X. A review on heterogeneous photocatalysis for environmental remediation: From semiconductors to modification strategies. *Chin. J. Catal* **2022**, *43* (2), 178−214.
(49) Zhang, M.; Wang, K.; Zeng, S.; Xu, Y.; Nie, W.; Chen, P.; Zhou, Y. Visible light-induced antibacterial effect of MoS2: Effect of the synthesis methods. *Chem. Eng. J.* **2021**, *411*, 128517.
(50) Wang, W.; Zhang, J.; Chen, T.; Sun, J.; Ma, X.; Wang, Y.; Wang, J.; Xie, Z. Preparation of TiO2-modified Biochar and its Characteristics of Photo-catalysis Degradation for Enrofloxacin. *Sci. Rep* **2020**, *10* (1), 6588.

https://doi.org/10.1021/acsomega.2c00523
ACS Omega 2022, 7, 12158−12170

(51) Huang, P.; Luan, J. Synthesis of a GaOOH/ZnBiTaO5 heterojunction photocatalyst with enhanced photocatalytic performance toward enrofloxacin. *RSC Adv.* **2020**, *10* (8), 4286−4292.
(52) Wang, A.; Wang, H.; Deng, H.; Wang, S.; Shi, W.; Yi, Z.; Qiu, R.; Yan, K. Controllable synthesis of mesoporous manganese oxide microsphere efficient for photo-Fenton-like removal of fluoroquinolone antibiotics. *Appl. Catal., B* **2019**, *248*, 298−308.
(53) Chen, Z.; Chen, X.; Di, J.; Liu, Y.; Yin, S.; Xia, J.; Li, H. Graphene-like boron nitride modified bismuth phosphate materials for boosting photocatalytic degradation of enrofloxacin. *J. Colloid Interface Sci.* **2017**, *492*, 51−60.
(54) Sciscenko, I.; Arques, A.; Varga, Z.; Bouchonnet, S.; Monfort, O.; Brigante, M.; Mailhot, G. Significant role of iron on the fate and photodegradation of enrofloxacin. *Chemosphere* **2021**, *270*, 129791.
(55) Ge, L.; Na, G.; Zhang, S.; Li, K.; Zhang, P.; Ren, H.; Yao, Z. New insights into the aquatic photochemistry of fluoroquinolone antibiotics: Direct photodegradation, hydroxyl-radical oxidation, and antibacterial activity changes. *Sci. Total Environ.* **2015**, *527*−*528*, 12−17.
(56) Wang, J.; Wang, G.; Cheng, B.; Yu, J.; Fan, J. Sulfur-doped g-C3N4/TiO2 S-scheme heterojunction photocatalyst for Congo Red photodegradation. *Chin. J. Catal* **2021**, *42* (1), 56−68.
(57) Zhang, R.; Yu, Y.; Wang, H.; Du, J. Mesoporous TiO2/g-C3N4 composites with O-Ti-N bridge for improved visible-light photodegradation of enrofloxacin. *Sci. Total Environ.* **2020**, *724*, 138280.
(58) Lu, Z.; Chen, F.; He, M.; Song, M.; Ma, Z.; Shi, W.; Yan, Y.; Lan, J.; Li, F.; Xiao, P. Microwave synthesis of a novel magnetic imprinted TiO2 photocatalyst with excellent transparency for selective photodegradation of enrofloxacin hydrochloride residues solution. *Chem. Eng. J.* **2014**, *249*, 15−26.

https://doi.org/10.1021/acsomega.2c00523
ACS Omega 2022, 7, 12158−12170